
Factorized Implicit Global Convolution for Automotive Computational Fluid Dynamics Prediction

Chris Choy, Alexey Kamenev, Jean Kossaifi, Max Rietmann
Jan Kautz, Kamyar Azizzadenesheli

NVIDIA

Abstract

Computational Fluid Dynamics (CFD) is crucial for automotive design, requiring the analysis of large 3D point clouds to study how vehicle geometry affects pressure fields and drag forces. However, existing deep learning approaches for CFD struggle with the computational complexity of processing high-resolution 3D data. We propose Factorized Implicit Global Convolution (FIGConv), a novel architecture that efficiently solves CFD problems for very large 3D meshes with arbitrary input and output geometries. FIGConv achieves quadratic complexity $O(N^2)$, a significant improvement over existing 3D neural CFD models that require cubic complexity $O(N^3)$. Our approach combines Factorized Implicit Grids to approximate high-resolution domains, efficient global convolutions through 2D reparameterization, and a U-shaped architecture for effective information gathering and integration. We validate our approach on the industry-standard Ahmed body dataset and the large-scale DrivAerNet dataset. In DrivAerNet, our model achieves an R^2 value of 0.95 for drag prediction, outperforming the previous state-of-the-art by a significant margin. This represents a 40% improvement in relative mean squared error and a 70% improvement in absolute mean squared error over previous methods.

1 Introduction

The automotive industry stands at the forefront of technological advancement and is heavily relying on computational fluid dynamics (CFD) to optimize vehicle designs for enhanced aerodynamics and fuel efficiency. Accurate simulation of complex fluid dynamics around automotive geometries is crucial to achieving optimal performance. However, traditional numerical solvers, including finite difference and finite element methods, often prove computationally intensive and time-consuming, particularly when dealing with large-scale simulations, as encountered in CFD applications. The demand for efficient solutions in the automotive sector requires the exploration of innovative approaches to accelerate fluid dynamics simulations and overcome the limitations of current solvers.

In recent years, deep learning methodologies have emerged as promising tools in scientific computing, advancing traditional simulation techniques, in biochemistry [Jumper et al., 2021], seismology [Yang et al., 2021], climate change mitigation [Wen et al., 2023], and weather [Pathak et al., 2022, Lam et al., 2022] to name a few. In fluid dynamics, recent attempts have been made to develop domain-specific deep learning methods to emulate fluid flow evolution in 2D and 3D proof-of-concept settings [Jacob et al., 2021, Li et al., 2020b, Pfaff et al., 2020a, Kossaifi et al., 2023]. Although most of these works focused on solving problems using relatively low-resolution grids, industrial automotive CFD requires working with detailed meshes that contain millions of points.

To address the time-consuming and computationally intensive nature of conventional CFD solvers on detailed meshes, recent studies [Jacob et al., 2021, Li et al., 2023] have explored replacing CFD simulations with deep learning-based models to accelerate the process. In particular, Jacob et al. [2021] studies the DrivAer dataset [Heft et al., 2012], utilize Unet [Ronneberger et al., 2015] architectures, and aim to predict the car surface drag coefficient – the integration of surface pressure

and friction – directly by bypassing integration. Furthermore, the architecture is applied on 3D voxel grids that requires $O(N^3)$ complexity, forcing the method to scale only to low-resolution 3D grids. Li et al. [2023] propose a neural operator method for Ahmed body [Ahmed et al., 1984] car dataset and aims to predict the pressure function on the car surface. This approach utilizes graph embedding to a uniform grid and performs 3D global convolution through fast Fourier transform (FFT). Although, in principle, this method handles different girding, the FFT in the operator imposes a complexity of $O(N^3 \log N^3)$, which becomes computationally prohibitive as the size of the grid increases. Both methods face scalability challenges due to their cubic complexity, which severely limits their representational power for high-resolution simulations. Consequently, there is a pressing need for a specialized domain-inspired method capable of handling 3D fine-grained car geometries with meshes comprising tens of millions of vertices [Jacob et al., 2021]. Such massive datasets require a novel approach in both design and implementation.

In this work, we propose a new quadratic complexity neural CFD approach $O(N^2)$, significantly improving scalability over existing 3D neural CFD models that require cubic complexity $O(N^3)$. Our method outperforms the state-of-the-art by reducing the absolute mean squared error by 70%.

The key innovations of our approach include Factorized Implicit Grids and Factorized Implicit Convolution. With Factorized Implicit Grids, we approximate high-resolution domains using a set of implicit grids, each with one lower-resolution axis. For example, a domain $1k \times 1k \times 1k$ containing 10^9 elements can be represented by three implicit grids with dimensions $5 \times 1k \times 1k$, $1k \times 4 \times 1k$, and $1k \times 1k \times 3$. This reduces the total number of elements to only $5M + 4M + 3M = 12M$, a significant reduction from the original 10^9 . Our Factorized Implicit Convolution method approximates 3D convolutions using these implicit grids, employing reparameterization techniques to accelerate computations.

We validate our approach on two large-scale CFD datasets. DrivAerNet [Heft et al., 2012, Elrefaie et al., 2024] and Ahmed body dataset [Ahmed et al., 1984]. Our experiments focus on the prediction of surface pressure and drag coefficients. The results demonstrate that our network is an order of magnitude faster than existing methods while achieving state-of-the-art performance in both drag coefficient prediction and per-face pressure prediction.

2 Related Work

The integration of deep learning into CFD processes has led to significant research efforts. The graph neural operator is among the first methods to explore neural operators in various geometries and meshes [Li et al., 2020b]. The architectures based on graph neural networks [Ummenhofer et al., 2019, Sanchez-Gonzalez et al., 2020, Pfaff et al., 2020a], follow message passing and encounter similar computational challenges when dealing with realistic receptive fields. The u-shaped graph kernel, inspired by multipole methods and UNet [Ronneberger et al., 2015], offers an innovative approach to graph and operator learning [Li et al., 2020c]. However, the core computational challenges in 3D convolution remain nevertheless, even for FNO-based architectures that are widely deployed [Li et al., 2022, Pathak et al., 2022, Wen et al., 2023].

Deep learning models in computer vision, for example, UNet, have been used to predict fluid average properties, such as final drag, for the automotive industry [Jacob et al., 2021, Trinh et al., 2024]. Studies that incorporate signed distance functions (SDF) to represent geometry have gained attention in which CNNs are used as predictive models in CFD simulations [Guo et al., 2016, Bhatnagar et al., 2019]. The 3D representation of SDF inflicts significant computation costs on the 3D models, making them only scale to low-resolution SDF, missing the details in the fine-car geometries.

Beyond partial differential equations (PDE) and scientific computing, various deep learning models have been developed to deal with fine-detail 3D scenes and objects. In particular, for dense prediction tasks in 3D space, a network is tasked to make predictions for all voxels or points, for which 3D UNets have been widely used for, e.g., segmentation [Li et al., 2018, Atzmon et al., 2018, Hermosilla et al., 2018, Graham and van der Maaten, 2017, Choy et al., 2019]. However, many of these networks exhibit poor scalability due to the cubic complexity of memory and computation $O(N^3)$ or slow neighbor search.

Recently, decomposed representations for 3D – where multiple orthogonal 2D planes have been used to reconstruct 3D representation – have gained popularity due to their efficient representation and have been used in generation [Chan et al., 2022, Shue et al., 2023] and reconstruction [Chen et al.,

2022, Fridovich-Keil et al., 2023, Cao and Johnson, 2023]. This representation significantly reduces the memory complexity of implicit neural networks in 3D continuous planes. Despite relying on the decomposition of continuous planes and fitting a single neural network to a scene, this approach shares relevance with our factorized grid convolution approach.

Previous works in the deep learning literature, focusing on large-scale point clouds, range from the use of graph neural networks and pointnets to the u-shaped architectures along with advanced neighborhood search [Qi et al., 2017a, Hamilton et al., 2017, Wang et al., 2019, Choy et al., 2019, Shi et al., 2020]. However, these methods make assumptions that may not be valid when applied to CFD problems. For example, the subsampling approach is a prominent approach to deal with the social network, classification, and segmentation to gain robustness and accuracy. However, in the automotive industry, dropping points could lead to a loss of fine-details in the geometry, the vital component of fluid dynamics evolution and car design. There is a need for a dedicated domain-inspired method that can work directly on fine-grained car geometry with meshes composed of $100M$ vertices [Jacob et al., 2021], a massive size that requires a unique design and treatment.

2.1 Factorization

The factorization of weights in neural networks has been studied to reduce the computational complexity of deep learning models Panagakis et al. [2021]. It has been applied to various layers, including fully connected Novikov et al. [2015], and most recently, low-rank adaptation of transformers [Hu et al., 2021], and the training of neural operators [Kossaifi et al., 2024]. In the context of convolutions, the use of factorization was first proposed by Rigamonti et al. [2013]. This decomposition can be either implicit Chollet [2017], using separable convolutions, for instance [Jaderberg et al., 2014], or explicit, e.g., using CP [Astrid and Lee, 2017, Lebedev et al., 2015] or Tucker [Kim et al., 2016] decompositions. All of these methods fit within a more general framework of decomposition of the kernels, where the full kernel is expressed in a factorized form, and the convolution is replaced by a sequence of smaller convolutions with the factors of the decomposition [Kossaifi et al., 2020]. Here, in contrast, we propose to factorize the **domain**, not the kernel, which allows us to perform **parallel** global convolution while remaining computationally tractable. The advantages include parallelism and better numerical stability, since we do not chain many operations. Factorization of the domain can lead to efficient computation, but the challenge is to find an explicit representation of the domain (Sect. 3.2).

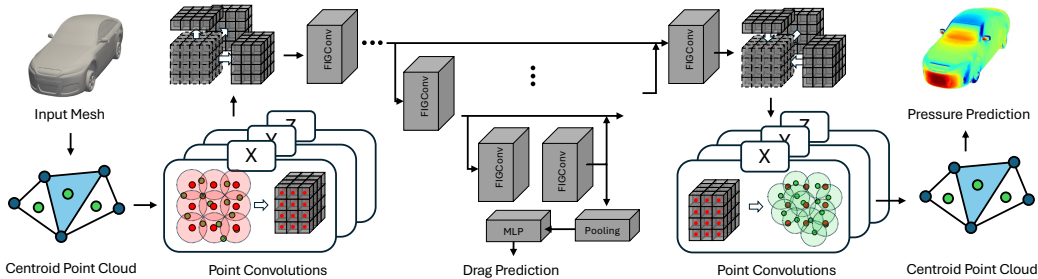


Figure 1: **FIGConvNet: ConvNet for drag prediction using FIG convolution blocks.** The encoder and decoder consist of a set of FIG convolution blocks and we connect the encoder and decoder with skip connections. The output of the encoder is used for drag prediction and the output of the decoder is used for pressure prediction.

3 Factorized Implicit Global ConvNet

In this section, we introduce our factorized implicit global convolution and discuss how we create implicit factorized representations, reparameterize the convolution, implement global convolution, and fuse implicit grids. We then present a convolution block using factorized implicit grids and build a U-shaped network architecture for the prediction of the pressure and drag coefficients. An overview diagram is provided in Fig. 1.

3.1 Factorized Implicit Grids

Our problem domain resides in a 3D space with an additional channel dimension, mathematically represented as $\mathcal{X} = \mathbb{R}^{H_{\max} \times W_{\max} \times D_{\max} \times C}$ with high spatial resolution. Explicitly representing an

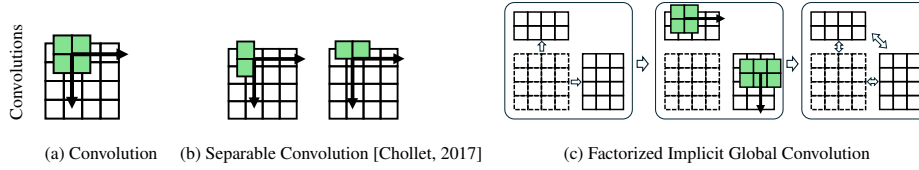


Figure 2: From left to right, we have a regular convolution, a separable convolution, and our proposed factorized implicit global (FIG) convolution. Regular Convolution: Requires $O(N^2k^2)$ computation and the convolution kernel is not global. Separable Convolution: Involves a **sequence** of $O(N^2k)$ convolutions, but the convolution kernel is still not global. FIG Convolution: Requires $O(Nk)$ computation in **parallel**, with convolution kernels that are global in one axis in the respective factorized domain.

instance of the domain $X \in \mathcal{X}$ is extremely costly in terms of memory and computation due to its large size. Instead, we propose using a set of factorized representations $\{F_m\}_{m=1}^M$, where M is the number of factorized representations. Each $F_m \in \mathbb{R}^{H_m \times W_m \times D_m \times C}$ has different dimensions, collectively approximating $X(\cdot) \approx \hat{X}(\cdot; \{F_m\}_{m=1}^M)$. These $\{F_m\}_{m=1}^M$ serve as **implicit representations** of the explicit representation X because we have to decode the implicit representations to represent the original high-resolution grid, and we refer to each F_m as a factorized implicit grid throughout this paper.

Mathematically, we use MLPs to project features from the factorized implicit grids $\{F_m\}_m$ to the explicit grid X :

$$X(v) \approx \hat{X}(v; \{F_m\}_m, \theta) = \prod_m^M f(v, F_m; \theta_m) \quad (1)$$

$$f(v, F_m; \theta_m) = \prod_{i=i_v}^{i_v+1} \prod_{j=j_v}^{j_v+1} \prod_{k=k_v}^{k_v+1} \text{MLP}(F_m[i, j, k], v; \theta_m), \quad (2)$$

where (i_v, j_v, k_v) is the smallest integer grid coordinate closest to the query coordinate $v \in \mathbb{R}^3$ and θ_m is the parameters of the MLP, which takes the concatenated features from the implicit grid F_m and position encoded v as an input.

To efficiently capture the high-resolution nature of the explicit grid X , we propose to make only one axis of low resolution $F_m \in \mathbb{R}^{H_m \times W_m \times D_m}$. For example, $F_1 \in \mathbb{R}^{4 \times W_{\max} \times D_{\max}}$ where $H_{\max} \gg 4$ and F_2, F_3 have low resolution W and D , respectively. Thus, the cardinality of X , $|X|$ is much greater than that of the factorized grids, $|X| \gg \sum_m |F_m|$. Formally, this low-resolution size is *rank* r of our factorized grid. For example, $F_x \in \mathbb{R}^{r_x \times W_{\max} \times D_{\max}}$, $F_y \in \mathbb{R}^{H_{\max} \times r_y \times D_{\max}}$, and $F_z \in \mathbb{R}^{H_{\max} \times W_{\max} \times r_z}$. In experiments, since we use 3D grids, the rank is a tuple of 3 values that we will denote as (r_x, r_y, r_z) , to represent the low-resolution components of (F_x, F_y, F_z) . In practice, we will use $r_i < 10$ in place of $H_{\max}, W_{\max}, D_{\max} > 100$, thus making the cardinality of factorized grids $|F_m|$ orders of magnitude smaller than that of $|X|$.

Note that when we use a rank of 1, that is, $(r_x, r_y, r_z) = (1, 1, 1)$, we have an implicit representation that resembles the triplane representation proposed in Chan et al. [2022] and Chen et al. [2022]. This is a special case of factorized implicit grids that are used for reconstruction without convolutions on the implicit grids, fusion (Sec. 3.4), or U-shape architecture (Sect. 3.6).

3.2 Factorized Implicit Convolution

In this section, we propose a convolution operation on factorized implicit grids. Specifically, we used a set of 3D convolutions on the factorized grids in parallel to approximate the 3D convolution on the explicit grid. Let N be the dimension of the high-resolution axis and K be the kernel size $N \gg K$. Then, the computational complexity of the original 3D convolution is $O(N^3K^3)$ and the computational complexity of the 3D convolution on factorized grids is $O(MN^2K^2r)$, where r is the dimension of the low-resolution axis, M is the number of factorized grids. Mathematically, we

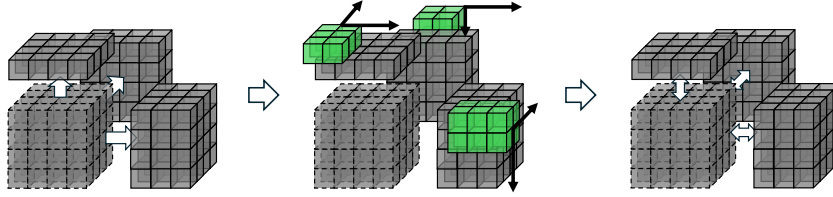


Figure 3: **Factorized Implicit Global Convolution 3D**: The FIG convolution first creates a set of voxel grids that factorizes the domain. This allows representing a high resolution voxel grid domain implicitly that can be computationally prohibitive to save explicitly. Then, a set of global convolution operations are applied in parallel to these voxel grids to capture the global context. Finally, the voxel grids are aggregated to predict the output.

have:

$$Y = \text{Conv3D}(X; W) \approx \prod_m Y_m = \prod_m f(\text{Conv3D}(X_m; W_m); \theta_m) \quad (3)$$

where Y and \hat{Y} are the output feature maps of the original and approximation, and W and W_m are the weights of the original and factorized implicit convolutions.

3.3 Efficient Global 3D Convolution through 2D Reparameterization

Large convolution kernels allow output features to incorporate broader context, leading to more accurate predictions [Peng et al., 2017, Huang et al., 2023]. Experimentally, we find larger kernel sizes yield higher accuracy on the test set (Tab. 2). However, large kernel sizes can be impractical due to their computational complexity, which increases cubically with respect to the kernel size. To enable a larger receptive field without making computation intractable, we propose a 2D reparameterization of 3D convolution that allows us to apply large convolution kernels while maintaining low computational complexity. Mathematically, any N-D convolution can be represented as a sum of vector-matrix multiplications since the convolution weights can be represented as a band matrix. Specifically, we focus on reparameterizing the 3D convolution to 2D convolution by flattening the low-resolution axis with the channel dimension to make use of the efficient **hardware acceleration** implemented in NVIDIA 2D convolution CUDA kernels. Mathematically, the 3D convolution on the flattened feature map is equivalent to 2D convolution with shifted kernel weights:

$$Y_m(i, j, k, c_o) = \sum_{c_{in}}^C \sum_{i', j', k'}^K X_m(i + i', j + j', k + k', c_{in}) W(i', j', k', c_{in}, c_o) \quad (4)$$

$$= \sum_{s=1}^{CK} \sum_{i', j'}^K X_m(i + i', j + j', k + \lfloor \frac{s}{C} \rfloor, s \bmod C) W_m(i', j', s \bmod C, c_o) \quad (5)$$

This is simply flattening of the last spatial dimension with the channel dimension for both X_m and W_m .¹ However, as we increase the kernel size $K \geq 2r - 1$ where r is the chosen rank, controlling the dimension of the low-resolution axis, we can reparameterize the convolution kernel into a matrix and replace the convolution with a matrix multiplication with the flattened input. For example, we can define a 1D convolution with kernel size $K = 3$ and the axis of size 2 (x_0, x_1) as:

$$\begin{bmatrix} y_0 \\ y_1 \end{bmatrix} = \begin{bmatrix} x_0 & x_1 & 0 \\ 0 & x_0 & x_1 \end{bmatrix} \begin{bmatrix} w_0 \\ w_1 \\ w_2 \end{bmatrix} \quad \text{1-D spatial convolution with 1 channel} \quad (6)$$

$$= \begin{bmatrix} w_0 & w_1 \\ w_1 & w_2 \end{bmatrix} \begin{bmatrix} x_0 \\ x_1 \end{bmatrix} \quad \text{reparameterization to 0-D space 2-vector matmul} \quad (7)$$

Using this reparameterization, we can convert a D dimensional convolution with large kernels to $D - 1$ -dimensional convolution with $C \times N_D$ channels where C is the original channel size and N_D

¹This is flattening operation `X_m.permute(0, 3, 4, 1, 2).reshape(B, D * C, H, W)` in torch to flatten the last dimension and permute the channel to be the second axis.

being the cardinality of the flattened dimension. In addition, the flattened kernel becomes a global convolution kernel along the low-dimensional axis as $K \geq 2r - 1$. Experimentally, we find that the larger convolution kernels outperform the smaller convolution kernels. However, if we do not use the reparameterization technique, the computation burden of the extra operations can outweigh the added benefit (Tab. 2). Note that this reparameterization does not change the underlying operation, but it reduces the computational complexity by removing redundant operations such as padding, truncation, and permutation involved in the 3D convolution as well as making use of the hardware acceleration of 2D convolution CUDA kernels. Lastly, we name the final reparameterized convolution on the factorized implicit grids the factorized implicit global convolution (FIG convolution) as we apply global convolution on the factorized grids.

3.4 Fusion of Factorized Implicit Grids

The convolution operation on the factorized implicit grids produces a set of feature maps $\{Y_m\}_m$ that, in combination, can represent the final feature map \hat{Y} of a 3D convolution that approximates Y , which we do not explicitly represent. Thus, if we apply the factorized implicit global convolution multiple times on the same factorized implicit grids, there would be no information exchange between the factorized representations. To enable information exchange between the factorized representations, we fuse the factorized representations after each convolution by aggregating features from the other factorized grids. Mathematically, we use trilinear interpolation to sample features from $M - 1$ factorized grids $\{F_{m'}\}_{m' \neq m}$ and add the sampled features to the target grid F_m by sampling from all the voxel locations v_{ijk} of F_m . We visualize the final 3D convolution operation in Fig. 3.

3.5 Continuous Convolution for Factorized Implicit Grids

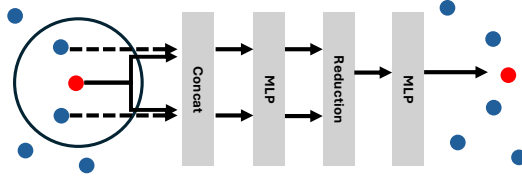


Figure 4: **Point Convolution:** The features from source and target nodes as well as offset are fed into an MLP to lift the features, which are then aggregated and projected back to the original feature space using an MLP.

We discussed how we perform global convolution on the factorized implicit grids. In this section, we discuss how we initialize the factorized implicit grids from an input 3D point cloud or a mesh. The traditional factorization of a large matrix of size N requires $O(N^3)$ computational complexity, where $A \approx \hat{A} = P^T Q$. However, this decomposition is not ideal for our case, where the resolution of the domain is extremely high. Instead, we propose learning the factorized implicit grids from the input point clouds or meshes rather than first converting to the explicit grid $X \in \mathbb{R}^{H_{\max} \times W_{\max} \times D_{\max} \times C}$ – where $H_{\max}, W_{\max}, D_{\max}$ are the maximum resolutions of the domain and C is the number of channels – and then factorize. We define a hyper parameter the number of factorized implicit grids M , as well as the size of the low-resolution axis r and create M factorized grids with different resolutions $\{F_m\}_m^M$, each with a different resolution $F_m \in \mathbb{R}^{H_m \times W_m \times D_m \times C}$. Then, we use a continuous convolution in each voxel center $v_{m,ijk}$ of F_m to update the feature of the voxel $f_{m,ijk}$ from the set of features f_n on point v_n of the point cloud. Note that the input mesh is converted to a point cloud where each point represent a face of a mesh. We use (i, j, k) to represent voxels and n to indicate points:

$$f_{m,ijk} = \text{MLP} \left(\sum_{n \in \mathcal{N}(v_{ijk})} \text{MLP}(f_n, v_n, v_{ijk}) \right), \quad \mathcal{N}(v, \Sigma) = \{i \mid \|\Sigma^{-1/2}(v_i - v)\| < 1\} \quad (8)$$

where $\mathcal{N}(v, \Sigma)$ is the set of points around v within an ellipsoid $(v_i - v)^T \Sigma^{-1} (v_i - v) < 1$ with covariance matrix $\Sigma \in \mathbb{R}^{3 \times 3}$ that defines the ellipsoid of neighborhood in physical domain. We use an ellipsoid rather than a sphere since the factorized grids have a rectangular shape due to one low resolution axis. Each mlp before and after the summation uses different parameters. To ensure the efficiency of the ellipsoid radius search, we leverage a hash grid provided by the GPU-acceleration library Warp [Macklin, 2022] and the pseudo-code is available in the Appendix.

3.6 UNet for Pressure and Drag Prediction

We combine factorized implicit global convolution with 2D reparameterization, fusion, and learned factorization to create a U-shaped ConvNet for drag prediction. Although drag can be directly regressed using a simple encoder architecture, the number of supervision points is extremely small compared to the number of parameters and the size of the dataset. Therefore, we add per-face pressure prediction as additional supervision, which is part of the ground truth since CFD simulation requires per-face pressure for drag simulation. We use the encoder output for drag prediction and the decoder output for pressure prediction. The architecture is visualized in Fig. 1.

4 Implementation Details and Training

We implement all baseline networks and FIG convnet using pytorch. In this section, we describe the implementation details of the FIG convnet and the training procedure.

4.1 Efficient Radius Search and Point Convolution

One of the most computationally intensive operations in our network is the radius search in Eq. 8 for which we leverage a hash grid to accelerate the search. We first create a hash grid using Warp [Macklin, 2022] with the voxel size as the radius. Then, we query all 27 neighboring voxels for each point in the point cloud and check if the point is within a unit sphere. For nonspherical neighborhoods, we scale the point cloud by the inverse of the covariance matrix Σ and check if the point is within the unit cube.

We save the neighborhood indices and the number of neighbors per point in a compressed sparse row matrix format (CSR) and use batched sparse matrix multiplication to perform convolution in Eq. 8. We provide a simple example of the radius search in the supplementary material.

4.2 Factorized Implicit Global Convolution

To implement 3D global convolution using factorized representations, we use a minimum of three factorized grids with one low-resolution axis. We first define the maximum resolution of the voxel grid that can represent the space explicitly, e.g. $512 \times 512 \times 512$. Then, we define the low resolution axis as r_i for each factorized grid. Note that r_i can be different for each factorized grid. For example, $512 \times 512 \times 2$, $512 \times 3 \times 512$, and $4 \times 512 \times 512$.

4.3 Training Procedure and Baseline Implementation

We train all networks using Adam Optimizer with a learning rate of 10^{-3} , a learning rate scheduler with $\gamma = 0.1$ and step size of 25 epochs, and batch size of 16 for 100 epochs on NVIDIA A100 80G GPUs. We use a single A100 if the batch size of 16 fits inside the memory and we use 2 GPUs with batch size 8 each if not to make sure that all experiments follow the same training configuration. The total training takes approximately 16 hours with two GPUs. For pressure prediction, we first normalize the pressure as all units are in the metric system and range widely. We denote \bar{P} as the normalized pressure where it has 0 mean and 1 standard deviation. For both pressure prediction and drag prediction, we use the same mean squared error as the loss function. Training loss is simply the sum of both: $(\hat{c}_d - c_d)^2 + \frac{1}{N} \sum_i (\hat{P}_i - \bar{P}_i)^2$ where $\hat{\cdot}$ denotes the prediction of \cdot and \bar{P}_i indicates the normalized pressure on the i -th face and N the number of faces. We use the same training procedure, loss with the same batch size, learning rate, and training epochs for all baseline networks to ensure fair comparison. There are many representative baselines, so we chose an open-source framework that supports a wide range of network architectures and is easy to implement new networks. Specifically, we use the OpenPoint library [Qian et al., 2022] to implement PointNet segmentation variants, DGCNN, and transformer networks. We provide the network configuration yaml files in the supplementary material.

5 Experiments

We evaluated our approach using two automotive computational fluid dynamics datasets, comparing it with strong baselines and state-of-the-art methods: **DrivAerNet** [Elrefaie et al., 2024]: Contains $4k$ meshes with CFD simulation results, including drag coefficients and mesh surface pressures. We adhere to the official evaluation metrics and the data split. **Ahmed body**: Comprise surface meshes with approximately $100k$ vertices, parameterized by height, width, length, ground clearance, slant angle, and fillet radius. Following [Li et al., 2023], we use about 10% of the data points for testing.

Table 1: **Performance on on DrivAerNet:** we evaluate drag coefficient c_d Mean Squared Error (MSE), Mean Absolute Error (MAE), Max Absolute Error (Max AE), coefficient of determination (R^2) of drag coefficient (c_d) prediction and inference time on the official test set. We evaluated the inference time on A100 single GPU. [†] numbers from the authors.

Model	c_d Mean SE (\downarrow)	c_d Mean AE (\downarrow)	c_d Max AE (\downarrow)	$c_d R^2$ (\uparrow)	Time (sec) (\downarrow)
PointNet++ [Qi et al., 2017b]	7.813E-5	6.755E-3	3.463E-2	0.896	0.200
DeepGCN [Li et al., 2019]	6.297E-5	6.091E-3	3.070E-2	0.916	0.151
MeshGraphNet [Pfaff et al., 2020b]	6.0E-5	6.08E-3	2.965E-2	0.917	0.25
AssaNet [Qian et al., 2021]	5.433E-5	5.81E-3	2.39E-2	0.927	0.11
PointNeXt [Qian et al., 2022]	4.577E-5	5.2E-3	2.41E-2	0.939	0.239
PointBERT [Yu et al., 2022]	6.334E-5	6.204E-3	2.767E-2	0.915	0.163
DrivAerNet DGCNN [Elrefaie et al., 2024] [†]	8.0E-5	6.91E-3	8.80E-3	0.901	0.52
FIGConvNet (Ours)	3.225E-5	4.423E-3	2.134E-2	0.957	0.051

Table 2: **Comparing Convolution Kernel Size (local and global) on DrivAerNet Normalized Pressure (\bar{P}) Prediction:** we evaluate Mean Squared Error (MSE), Mean Absolute Error (MAE), Max Absolute Error (Max AE), of normalized pressure and the coefficient of determination (R^2) of drag coefficient and inference time on the official test set. The local convolution suffers from long inference time. $(r_x, r_y, r_z) = (4, 4, 4)$ and kernel size $K \geq 2r - 1$ is global. (Sec. 3.3)

Kernel size	\bar{P} Mean SE (\downarrow)	\bar{P} Mean AE (\downarrow)	\bar{P} Max AE (\downarrow)	$c_d R^2$ (\uparrow)	Time (sec) (\downarrow)
$3 \times 3 \times 3$	0.046845	0.11895	5.95431	0.93	0.054
$5 \times 5 \times 5$	0.046364	0.11489	5.7173	0.943	0.061
$7 \times 7 \times 7$ (Global)	0.044959	0.1124	5.6795	0.955	0.079
$7 \times 7 \times 7$ (2D Reparameterization)	0.043818	0.11285	5.73351	0.957	0.051

The wind tunnel inlet velocity ranges from $10m/s$ to $70m/s$, which we include as an additional input to the network.

5.1 Experiment Setting

The car models in both data sets consist of triangular or quadrilateral meshes with faces and pressure values defined on vertices for the DrivAerNet and faces on the Ahmed body data set. As the network cannot directly process a triangular or quadrilateral face, we convert a face to a centroid point and predict the pressure on these centroid vertices for the Ahmed body dataset.

To gauge the performance of our proposed network, we considered a large number of state-of-the-art dense prediction network architectures (e.g., semantic segmentation) for comparison including Dynamic Graph CNN (DGCNN) [Wang et al., 2019], PointTransformers [Zhao et al., 2021], PointCNN [Qi et al., 2017a, Li et al., 2018], and geometry-informed neural operator(GINO)[Li et al., 2023]. For the DrivAerNet dataset, we follow the DrivAerNet [Elrefaie et al., 2024] and sample N number of points from the point cloud and evaluate the MSE, MAE, Max Error, and the coefficient of determination R^2 of drag prediction. For the Ahmed body dataset, we follow the same setting as [Li et al., 2023] and evaluate the pressure prediction.

5.2 Results on DrivAerNet

Table 1 presents the performance comparison of various methods in the DrivAerNet dataset. Our FIGConvNet outperforms all state-of-the-art methods in drag coefficient prediction while maintaining fast inference times. PointNet variants (e.g., PointNet++, PointNeXt) perform well compared to transformer-based networks like PointBERT, likely due to the dataset’s small size. For all baselines except DrivAerNet DGCNN, we incorporate both pressure prediction and drag coefficient prediction losses.

We analyze the impact of the size of the convolution kernel on the prediction of pressure (Table 2). Larger kernels approach global convolution, but lead to performance saturation and slower inference. Our reparameterized 3D convolution achieves comparable performance with improved speed.

Figure 5b visualizes the ground truth versus predicted drag coefficients, demonstrating the network’s ability to capture the distribution accurately. Figure 5a shows the effect of the sample point count on the precision of the prediction, revealing robustness over a wide range but potential overfitting with very high point counts. Qualitative pressure predictions are shown in Figure 6.

To assess the impact of factorized grid dimensions, we varied grid sizes (Table 3). Larger grids improved the accuracy of pressure prediction, but degraded the coefficient of determination (R^2) of the drag coefficient and increased the inference time.

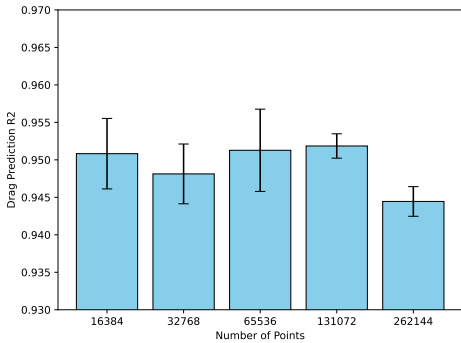
Lastly, we remove the feature fusion between factorized grids proposed in Sect. 3.4. We observe that having no fusion in FIG convolution degrades performance but the gap is smaller when the grid (r_x, r_y, r_z) is larger. This suggests that while fusion remains important, its significance decreases with increasing grid size.

Table 3: **Choosing the rank: impact of the choice of on DrivAerNet on performance:** we evaluate normalized pressure \bar{P} Mean Squared Error (MSE), Mean Absolute Error (MAE), Max Absolute Error (Max AE), coefficient of determination (R^2) of drag coefficient c_d and inference time on the official test set. We trained for only 50 epochs for this experiment. Note that the car is facing +x axis and is the longest while -z is the gravity axis and is the shortest. See Sec. 3.1 for (r_x, r_y, r_z) definition.

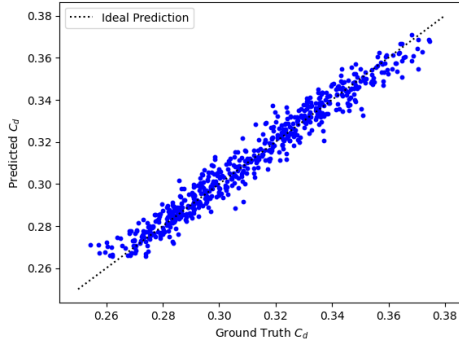
(r_x, r_y, r_z)	\bar{P} Mean SE (\downarrow)	\bar{P} Mean AE (\downarrow)	\bar{P} Max AE (\downarrow)	$c_d R^2$ (\uparrow)	Time (sec) (\downarrow)
(1, 1, 1)	0.05278	0.1275	5.8266	0.9328	0.0305
(3, 2, 2)	0.05199	0.1250	5.8284	0.9249	0.0396
(5, 3, 2)	0.05131	0.1223	6.2350	0.8735	0.0399
(10, 6, 4)	0.05079	0.1221	5.6506	0.9243	0.0493
(10, 10, 10)	0.04999	0.1254	5.5343	0.8926	0.0610

Table 4: Impact of the factorized grid fusion (Sec. 3.4) on DrivAerNet: we evaluate normalized pressure \bar{P} Mean Squared Error (MSE), Mean Absolute Error (MAE), Max Absolute Error (Max AE), coefficient of determination (R^2) of drag coefficient c_d , and inference time on the official test set. We trained for 50 epochs for this experiment. For no communication rows, we set the fusion layer in Sec. 3.4 to be identity and kept all the rest of the network the same.

(r_x, r_y, r_z)	\bar{P} Mean SE (\downarrow)	\bar{P} Mean AE (\downarrow)	\bar{P} Max AE (\downarrow)	$c_d R^2$ (\uparrow)	Time (sec) (\downarrow)
(3, 2, 2)	0.05199	0.1250	5.8284	0.9249	0.0396
(3, 2, 2) No Fusion	0.053455	0.12683	6.28512	0.90413	0.0361
(5, 3, 2)	0.05131	0.1223	6.2350	0.8735	0.0399
(5, 3, 2) No Fusion	0.052921	0.12287	6.02101	0.88638	0.0451



(a) Number of Sample Points on Drag Prediction: The networks are robust to the number of sample points used for drag prediction.



(b) Drag prediction vs. Ground truth drag on DrivAerNet. The drag prediction closely matches the drag ground truth with R^2 of 0.95.

5.3 Results on Ahmed body

Table 5 compares the performance of our method in the Ahmed body data set with state-of-the-art approaches Li et al. [2023], reporting normalized pressure MSE and model size. Although GINO outperforms UNet and FNO, it achieves only 9% pressure error. In contrast, our method attains a significantly lower normalized pressure error of 0.89% with a smaller model footprint.

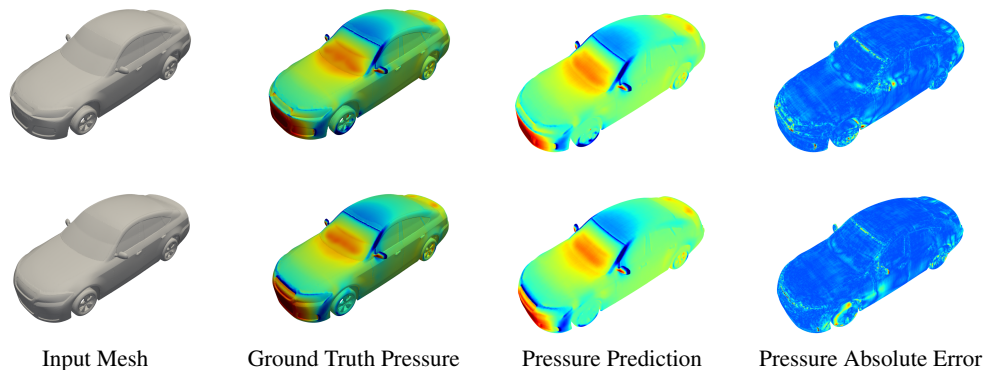


Figure 6: **Normalized Pressure Prediction and Error Visualization on DrivAerNet.** Our network predicts both drag coefficients and per vertex pressure. We visualize the ground truth pressure and prediction along with the absolute error of the pressure. Note that the pressures are normalized to highlight the errors clearly.

Table 5: **Ahmed Body Per Vertex Pressure Prediction Error** measured the normalized L2 pressure error per vertex on the test set. The top three rows are from Li et al. [2023].

Model	Pressure Error	Model Size (MB)
UNet (interp)	11.16%	0.13
FNO (interp) Li et al. [2020a]	12.59%	924.34
GINO Li et al. [2023]	9.01%	923.63
FIGConvNet (Ours)	0.89%	68.29

We further analyze the impact of grid resolution on network performance (Table 6). Our approach demonstrates robust pressure prediction across a wide range of grid resolutions, even with small grids. However, we observe that very high grid resolutions lead to overfitting on training data, resulting in decreased test performance.

6 Conclusion and Limitations

In this work, we proposed a deep learning method for automotive drag coefficient prediction using a network with factorized implicit global convolutions. This approach efficiently captures the global context of the geometry, outperforming state-of-the-art methods on two automotive CFD datasets. On the DrivAerNet dataset, our method achieved an R^2 value of 0.95 for drag coefficient prediction, while on the Ahmed body dataset, it attained a normalized pressure error of 0.89%.

However, our approach has some limitations. The FIG ConvNet directly regresses the drag coefficient without incorporating physics-based constraints, which could lead to overfitting and poor generalization to unseen data. Additionally, our method is currently limited to the automotive domain with a restricted model design, potentially limiting its applicability to other fields. Looking ahead, we plan to address these limitations and further improve our model. Future work will focus on incorporating physics-based constraints such as Reynolds number and wall shear stress to enhance generalization.

References

- Syed R Ahmed, G Ramm, and Gunter Faltn. Some salient features of the time-averaged ground vehicle wake. *SAE transactions*, pages 473–503, 1984.
- Marcella Astrid and Seung-Ik Lee. Cp-decomposition with tensor power method for convolutional neural networks compression. *CoRR*, abs/1701.07148, 2017.
- Matan Atzmon, Haggai Maron, and Yaron Lipman. Point convolutional neural networks by extension operators. *arXiv preprint arXiv:1803.10091*, 2018.
- Saakaar Bhatnagar, Yaser Afshar, Shaowu Pan, Karthik Duraisamy, and Shailendra Kaushik. Prediction of aerodynamic flow fields using convolutional neural networks. *Computational Mechanics*, 64:525–545, 2019.
- Ang Cao and Justin Johnson. Hexplane: A fast representation for dynamic scenes. In *Proceedings of the IEEE/CVF Conference on Computer Vision and Pattern Recognition*, pages 130–141, 2023.
- Eric R Chan, Connor Z Lin, Matthew A Chan, Koki Nagano, Boxiao Pan, Shalini De Mello, Orazio Gallo, Leonidas J Guibas, Jonathan Tremblay, Sameh Khamis, et al. Efficient geometry-aware 3d generative adversarial networks. In *Proceedings of the IEEE/CVF Conference on Computer Vision and Pattern Recognition*, pages 16123–16133, 2022.
- Angel X Chang, Thomas Funkhouser, Leonidas Guibas, Pat Hanrahan, Qixing Huang, Zimo Li, Silvio Savarese, Manolis Savva, Shuran Song, Hao Su, et al. Shapenet: An information-rich 3d model repository. *arXiv preprint arXiv:1512.03012*, 2015.
- Anpei Chen, Zexiang Xu, Andreas Geiger, Jingyi Yu, and Hao Su. Tensorf: Tensorial radiance fields. In *European Conference on Computer Vision (ECCV)*, 2022.
- François Chollet. Xception: Deep learning with depthwise separable convolutions. In *Proceedings of the IEEE conference on computer vision and pattern recognition*, pages 1251–1258, 2017.
- Christopher Choy, JunYoung Gwak, and Silvio Savarese. 4d spatio-temporal convnets: Minkowski convolutional neural networks. In *Proceedings of the IEEE/CVF conference on computer vision and pattern recognition*, pages 3075–3084, 2019.
- Mohamed Elrefaie, Angela Dai, and Faez Ahmed. Drivaernet: A parametric car dataset for data-driven aerodynamic design and graph-based drag prediction. *arXiv preprint arXiv:2403.08055*, 2024.
- Joel H Ferziger, Milovan Perić, and Robert L Street. *Computational methods for fluid dynamics*. springer, 2019.
- Sara Fridovich-Keil, Giacomo Meanti, Frederik Rahbæk Warburg, Benjamin Recht, and Angjoo Kanazawa. K-planes: Explicit radiance fields in space, time, and appearance. In *CVPR*, 2023.
- Benjamin Graham and Laurens van der Maaten. Submanifold sparse convolutional networks. *arXiv preprint arXiv:1706.01307*, 2017.
- Xiaoxiao Guo, Wei Li, and Francesco Iorio. Convolutional neural networks for steady flow approximation. In *Proceedings of the 22nd ACM SIGKDD international conference on knowledge discovery and data mining*, pages 481–490, 2016.
- Will Hamilton, Zhitao Ying, and Jure Leskovec. Inductive representation learning on large graphs. *Advances in neural information processing systems*, 30, 2017.
- Angelina I Heft, Thomas Indinger, and Nikolaus A Adams. Introduction of a new realistic generic car model for aerodynamic investigations. Technical report, SAE Technical Paper, 2012.
- P. Hermosilla, T. Ritschel, P-P Vazquez, A. Vinacua, and T. Ropinski. Monte carlo convolution for learning on non-uniformly sampled point clouds. *ACM Transactions on Graphics (Proceedings of SIGGRAPH Asia 2018)*, 2018.

- Edward J. Hu, Yelong Shen, Phillip Wallis, Zeyuan Allen-Zhu, Yuanzhi Li, Shean Wang, and Weizhu Chen. Lora: Low-rank adaptation of large language models. *CoRR*, abs/2106.09685, 2021. URL <https://arxiv.org/abs/2106.09685>.
- Tianjin Huang, Lu Yin, Zhenyu Zhang, Li Shen, Meng Fang, Mykola Pechenizkiy, Zhangyang Wang, and Shiwei Liu. Are large kernels better teachers than transformers for convnets? In *International Conference on Machine Learning*, pages 14023–14038. PMLR, 2023.
- Sam Jacob Jacob, Markus Mrosek, Carsten Othmer, and Harald Köstler. Deep learning for real-time aerodynamic evaluations of arbitrary vehicle shapes. *arXiv preprint arXiv:2108.05798*, 2021.
- M. Jaderberg, A. Vedaldi, and A. Zisserman. Speeding up convolutional neural networks with low rank expansions. In *British Machine Vision Conference*, 2014.
- Hrvoje Jasak, Aleksandar Jemcov, Zeljko Tukovic, et al. Openfoam: A c++ library for complex physics simulations. In *International workshop on coupled methods in numerical dynamics*, volume 1000, pages 1–20, 2007.
- John Jumper, Richard Evans, Alexander Pritzel, Tim Green, Michael Figurnov, Olaf Ronneberger, Kathryn Tunyasuvunakool, Russ Bates, Augustin Žídek, Anna Potapenko, et al. Highly accurate protein structure prediction with alphafold. *Nature*, 596(7873):583–589, 2021.
- Joseph Katz. *Automotive aerodynamics*. John Wiley & Sons, 2016.
- Yong-Deok Kim, Eunhyeok Park, Sungjoo Yoo, Taelim Choi, Lu Yang, and Dongjun Shin. Compression of deep convolutional neural networks for fast and low power mobile applications. *ICLR*, 2016.
- J. Kossaifi, A. Toisoul, A. Bulat, Y. Panagakis, T. M. Hospedales, and M. Pantic. Factorized higher-order cnns with an application to spatio-temporal emotion estimation. In *2020 IEEE/CVF Conference on Computer Vision and Pattern Recognition (CVPR)*, pages 6059–6068, Los Alamitos, CA, USA, jun 2020. IEEE Computer Society. doi: 10.1109/CVPR42600.2020.00610. URL <https://doi.ieeecomputersociety.org/10.1109/CVPR42600.2020.00610>.
- Jean Kossaifi, Nikola Kovachki, Kamyar Azizzadenesheli, and Anima Anandkumar. Multi-grid tensorized fourier neural operator for high-resolution pdes, 2023.
- Jean Kossaifi, Nikola Borislavov Kovachki, Kamyar Azizzadenesheli, and Anima Anandkumar. Multi-grid tensorized fourier neural operator for high- resolution PDEs. *Transactions on Machine Learning Research*, 2024. ISSN 2835-8856. URL <https://openreview.net/forum?id=AWiD1063bH>.
- Remi Lam, Alvaro Sanchez-Gonzalez, Matthew Willson, Peter Wirnsberger, Meire Fortunato, Alexander Pritzel, Suman Ravuri, Timo Ewalds, Ferran Alet, Zach Eaton-Rosen, et al. Graphcast: Learning skillful medium-range global weather forecasting. *arXiv preprint arXiv:2212.12794*, 2022.
- Vadim Lebedev, Yaroslav Ganin, Maksim Rakhuba, Ivan V. Oseledets, and Victor S. Lempitsky. Speeding-up convolutional neural networks using fine-tuned cp-decomposition. In *ICLR*, 2015.
- Guohao Li, Matthias Muller, Ali Thabet, and Bernard Ghanem. Deepgcn: Can gcns go as deep as cnns? In *Proceedings of the IEEE/CVF international conference on computer vision*, pages 9267–9276, 2019.
- Yangyan Li, Rui Bu, Mingchao Sun, Wei Wu, Xinhan Di, and Baoquan Chen. Pointcnn: Convolution on x-transformed points. *Advances in neural information processing systems*, 31, 2018.
- Zongyi Li, Nikola Kovachki, Kamyar Azizzadenesheli, Burigede Liu, Kaushik Bhattacharya, Andrew Stuart, and Anima Anandkumar. Fourier neural operator for parametric partial differential equations. *arXiv preprint arXiv:2010.08895*, 2020a.
- Zongyi Li, Nikola Kovachki, Kamyar Azizzadenesheli, Burigede Liu, Kaushik Bhattacharya, Andrew Stuart, and Anima Anandkumar. Neural operator: Graph kernel network for partial differential equations. *arXiv preprint arXiv:2003.03485*, 2020b.

- Zongyi Li, Nikola Kovachki, Kamyar Azizzadenesheli, Burigede Liu, Andrew Stuart, Kaushik Bhattacharya, and Anima Anandkumar. Multipole graph neural operator for parametric partial differential equations. *Advances in Neural Information Processing Systems*, 33, 2020c.
- Zongyi Li, Daniel Zhengyu Huang, Burigede Liu, and Anima Anandkumar. Fourier neural operator with learned deformations for pdes on general geometries. *arXiv preprint arXiv:2207.05209*, 2022.
- Zongyi Li, Nikola B. Kovachki, Chris Choy, Boyi Li, Jean Kossaifi, Shourya Prakash Otta, Mohammad Amin Nabian, Maximilian Stadler, Christian Hundt, Kamyar Azizzadenesheli, et al. Geometry-informed neural operator for large-scale 3d pdes. *arXiv preprint arXiv:2309.00583*, 2023.
- Miles Macklin. Warp: A high-performance python framework for gpu simulation and graphics. <https://github.com/nvidia/warp>, March 2022. NVIDIA GPU Technology Conference (GTC).
- Alexander Novikov, Dmitry Podoprikin, Anton Osokin, and Dmitry Vetrov. Tensorizing neural networks. In *Neural Information Processing Systems*, 2015.
- Yannis Panagakis, Jean Kossaifi, Grigorios G. Chrysos, James Oldfield, Mihalis A. Nicolaou, Anima Anandkumar, and Stefanos Zafeiriou. Tensor methods in computer vision and deep learning. *Proceedings of the IEEE*, 109(5):863–890, 2021. doi: 10.1109/JPROC.2021.3074329.
- Jaideep Pathak, Shashank Subramanian, Peter Harrington, Sanjeev Raja, Ashesh Chattopadhyay, Morteza Mardani, Thorsten Kurth, David Hall, Zongyi Li, Kamyar Azizzadenesheli, et al. Fourcast-net: A global data-driven high-resolution weather model using adaptive fourier neural operators. *arXiv preprint arXiv:2202.11214*, 2022.
- Chao Peng, Xiangyu Zhang, Gang Yu, Guiming Luo, and Jian Sun. Large kernel matters—improve semantic segmentation by global convolutional network. In *Proceedings of the IEEE conference on computer vision and pattern recognition*, pages 4353–4361, 2017.
- Tobias Pfaff, Meire Fortunato, Alvaro Sanchez-Gonzalez, and Peter W Battaglia. Learning mesh-based simulation with graph networks. *arXiv preprint arXiv:2010.03409*, 2020a.
- Tobias Pfaff, Meire Fortunato, Alvaro Sanchez-Gonzalez, and Peter W. Battaglia. Learning mesh-based simulation with graph networks. *arXiv preprint arXiv:2010.03409*, 2020b.
- Charles R Qi, Hao Su, Kaichun Mo, and Leonidas J Guibas. Pointnet: Deep learning on point sets for 3d classification and segmentation. In *Proceedings of the IEEE conference on computer vision and pattern recognition*, pages 652–660, 2017a.
- Charles Ruizhongtai Qi, Li Yi, Hao Su, and Leonidas J Guibas. Pointnet++: Deep hierarchical feature learning on point sets in a metric space. *Advances in neural information processing systems*, 30, 2017b.
- Guocheng Qian, Hasan Hammoud, Guohao Li, Ali Thabet, and Bernard Ghanem. Assanet: An anisotropic separable set abstraction for efficient point cloud representation learning. *Advances in Neural Information Processing Systems*, 34:28119–28130, 2021.
- Guocheng Qian, Yuchen Li, Houwen Peng, Jinjie Mai, Hasan Hammoud, Mohamed Elhoseiny, and Bernard Ghanem. Pointnext: Revisiting pointnet++ with improved training and scaling strategies. *Advances in Neural Information Processing Systems*, 35:23192–23204, 2022.
- R. Rigamonti, A. Sironi, V. Lepetit, and P. Fua. Learning separable filters. In *2013 IEEE Conference on Computer Vision and Pattern Recognition*, June 2013. doi: 10.1109/CVPR.2013.355.
- Olaf Ronneberger, Philipp Fischer, and Thomas Brox. U-net: Convolutional networks for biomedical image segmentation. In *Medical Image Computing and Computer-Assisted Intervention—MICCAI 2015: 18th International Conference, Munich, Germany, October 5–9, 2015, Proceedings, Part III 18*, pages 234–241. Springer, 2015.
- Alvaro Sanchez-Gonzalez, Jonathan Godwin, Tobias Pfaff, Rex Ying, Jure Leskovec, and Peter Battaglia. Learning to simulate complex physics with graph networks. In *International conference on machine learning*, pages 8459–8468. PMLR, 2020.

- Shaoshuai Shi, Chaoxu Guo, Li Jiang, Zhe Wang, Jianping Shi, Xiaogang Wang, and Hongsheng Li. Pv-rcnn: Point-voxel feature set abstraction for 3d object detection. In *Proceedings of the IEEE/CVF conference on computer vision and pattern recognition*, pages 10529–10538, 2020.
- J. Ryan Shue, Eric Ryan Chan, Ryan Po, Zachary Ankner, Jiajun Wu, and Gordon Wetzstein. 3d neural field generation using triplane diffusion. In *Proceedings of the IEEE/CVF Conference on Computer Vision and Pattern Recognition (CVPR)*, pages 20875–20886, June 2023.
- Thanh Luan Trinh, Fangge Chen, Takuya Nanri, and Kei Akasaka. 3d super-resolution model for vehicle flow field enrichment. In *Proceedings of the IEEE/CVF Winter Conference on Applications of Computer Vision*, pages 5826–5835, 2024.
- Nobuyuki Umetani and Bernd Bickel. Learning three-dimensional flow for interactive aerodynamic design. *ACM Transactions on Graphics (TOG)*, 37(4):1–10, 2018.
- Benjamin Ummenhofer, Lukas Prantl, Nils Thuerey, and Vladlen Koltun. Lagrangian fluid simulation with continuous convolutions. In *International Conference on Learning Representations*, 2019.
- Max Varney, Martin Passmore, Felix Wittmeier, and Timo Kuthada. Experimental data for the validation of numerical methods: Drivaer model. *Fluids*, 5(4):236, 2020.
- Yue Wang, Yongbin Sun, Ziwei Liu, Sanjay E Sarma, Michael M Bronstein, and Justin M Solomon. Dynamic graph cnn for learning on point clouds. *ACM Transactions on Graphics (tog)*, 38(5): 1–12, 2019.
- Gege Wen, Zongyi Li, Qirui Long, Kamyar Azizzadenesheli, Anima Anandkumar, and Sally M Benson. Real-time high-resolution co 2 geological storage prediction using nested fourier neural operators. *Energy & Environmental Science*, 16(4):1732–1741, 2023.
- Yan Yang, Angela F Gao, Jorge C Castellanos, Zachary E Ross, Kamyar Azizzadenesheli, and Robert W Clayton. Seismic wave propagation and inversion with neural operators. *The Seismic Record*, 1(3):126–134, 2021.
- Xumin Yu, Lulu Tang, Yongming Rao, Tiejun Huang, Jie Zhou, and Jiwen Lu. Point-bert: Pre-training 3d point cloud transformers with masked point modeling. In *Proceedings of the IEEE/CVF conference on computer vision and pattern recognition*, pages 19313–19322, 2022.
- Hengshuang Zhao, Li Jiang, Jiaya Jia, Philip HS Torr, and Vladlen Koltun. Point transformer. In *Proceedings of the IEEE/CVF international conference on computer vision*, pages 16259–16268, 2021.

A Appendix

B Datasets

The foundation of CFD in the automotive industry provides insight into design and engineering. The comprehensive previous texts provide a solid overview of computational methods in fluid dynamics and dedicate a comprehensive overview of traditional CFD techniques [Ferziger et al., 2019] along with specification in automotive aerodynamics, also instrumental in understanding the principles [Katz, 2016]. Solvers, such as OpenFOAM, a GPU-accelerated open-source solver, along with commercialized licensed solvers are widely used for solving CFD equations in automotive simulations [Jasak et al., 2007].

Such simulations consist of two main components, i) car designs, complex geometry often developed special software, and ii) running large scale computation to solve multivariate coupled equations. Significant advancements have been achieved by the Ahmed body shape [Ahmed et al., 1984], a generic car model simple enough to enable high-fidelity industry standard simulations while retaining the main features characterizing the flow of modern cars. Since then, attempts have been made to improve the realism of the shapes. Shape-net [Chang et al., 2015] in particular has provided a valuable resource for simple CFD simulations of cars [Umetani and Bickel, 2018]. Extending Ahmed’s body setting, the DrivAer data set introduces more complex and realistic car geometries [Heft et al., 2012], with subsequent efforts, producing large-scale aerodynamics simulations on such geometries [Varney et al., 2020]. On such dataset, prior work attempts to predict car surface drag coefficients directly by bypassing the surface pressure prediction, pioneered by Jacob et al. [2021]. However, this approach deploys an architecture applied to 3D voxel grids, forcing the method to scale only to low-resolution 3D grid version of the data. The lack of resolution obscures the fine details of geometry, causing the network to predict the same results for cars with different information. This is in contrast to our work that predicts pressure fields on large scales and detailed meshes.

Ahmed body consists of generic automotive geometries [Ahmed et al., 1984], simple enough to enable high-fidelity industry standard simulations but retaining the main features characterizing the flow of modern cars. It was generated and used in previous studies [Li et al., 2023] and contains simulations with various wind-tunnel inlet velocities.

The Ahmed body data set, generated using vehicle aerodynamic simulation in Ahmed body shapes [Ahmed et al., 1984], consists of steady-state simulation of OpenFOAM solver in 3D meshes each with $10M$ vertices parameterized by height, width, length, ground clearance, slant angle, and fillet radius. The data set is generated and used in previous studies [Li et al., 2023] and contains GPU-accelerated simulations with surface mesh sizes of $100k$ on more than 500 car geometries, each taking 7-19 hours. We follow the same setting as this study using the 10% shape testing. The dataset is proprietary from NVIDIA Corp. Following this work, both of the deployed datasets are in the process of being made publicly available for further research.

Table 6: **Ahmed body Controlled Experiment** We vary the grid resolution and kernel size for analysis. (r_x, r_y, r_z) is $(6, 2, 2)$ (Sec. 3.1) e.g. The three grid resolutions we used for the first three rows are $6 \times 280 \times 180$, $560 \times 2 \times 180$, $560 \times 208 \times 2$.

Max Resolution	Kernel Size	Pressure Error	Model Size (MB)
$560 \times 208 \times 180$	3	3.40%	105.0
	7	3.31%	417.1
	11	2.56%	979.7
$280 \times 104 \times 90$	3	2.89%	105.0
	7	3.05%	417.1
	11	2.93%	979.7
$140 \times 42 \times 45$	9	1.65%	667.29
	11	2.59%	979.7

DrivAerNet datasets is the parametric extension of DrivAer datasets. DriveAer car geometries are more complex real-world automotive designs used by the automotive industry and solver development [Heft et al., 2012]. Solving the aerodynamic equation for such geometries is a challenging task, and GPU-accelerated solvers are used to provide fast and accurate solvers, generating training data for deep learning purposes [Varney et al., 2020, Jacob et al., 2021]. To train our model on the

DrivAer dataset, and to demonstrate the applicability of our approach to real-world applications, we use industry simulations from Jacob et al. [2021]. DrivAerNet with 50 parameters in the design space. The dataset consists of 4000 data points generated using Reynolds-average Navier-Stokes (RANS) formulation on OpenFoam solver on 0.5M mesh faces.

B.1 Baseline Network Configurations

We list the network configurations used in the experiment in the appendix. We use OpenPoint Qian et al. [2022] for the baseline implementation and, with configuration, you can specify the network architecture.

B.2 Baseline Implementations

We use the OpenPoint, an open-source 3D point cloud library [Qian et al., 2022] to implement PointNet++ [Qi et al., 2017b], DeepGCN [Li et al., 2019], AssaNet [Qian et al., 2021], PointNeXt [Qian et al., 2022], and PointBERT [Yu et al., 2022]. In this section, we share the network architecture configuration used in the experiment.

```

NAME: BaseSeg
encoder_args:
  NAME: PointNet2Encoder
  in_channels: 3
  width: null
  strides: [2, 4, 1]
  mlps: [[[64, 64, 128]],
          [[128, 128, 256]],
          [[256, 512, 512]]]
  layers: 3
  use_res: False
  radius: 0.05
  num_samples: 32
  sampler: fps
  aggr_args:
    NAME: 'convpool'
    feature_type: 'dp_fj'
    anisotropic: False
    reduction: 'max'
  group_args:
    NAME: 'ballquery'
  conv_args:
    order: conv-norm-act
  act_args:
    act: 'relu'
  norm_args:
    norm: 'bn'
decoder_args:
  NAME: PointNet2Decoder
  fp_mlps: [[128, 128], [256, 128], [512, 128]]

```

Listing 1: PointNet++ Configuration

```

NAME: BaseSeg
encoder_args:
  NAME: DeepGCN
  in_channels: 3
  channels: 64
  n_classes: 256
  emb_dims: 256
  n_blocks: 14
  conv: 'edge'
  block: 'res'
  k: 9
  epsilon: 0.0
  use_stochastic: False
  use_dilation: True
  dropout: 0
  norm_args: {'norm': 'in'}
  act_args: {'act': 'relu'}

```

Listing 2: DeepGCN Configuration

```

NAME: BaseSeg
encoder_args:
  NAME: PointNet2Encoder
  in_channels: 3
  strides: [4, 4, 4, 4]
  blocks: [3, 3, 3, 3]
  width: 128
  width_scaling: 3
  double_last_channel: False
  layers: 3
  use_res: True
  query_as_support: True
  mlps: null
  stem_conv: True
  stem_aggr: True
  radius: [[0.1, 0.2], [0.2, 0.4], [0.4, 0.8], [0.8, 1.6]]
  num_samples: [[16, 32], [16, 32], [16, 32], [16, 32]]
  sampler: fps
  aggr_args:
    NAME: 'ASSA'
    feature_type: 'assa'
    anisotropic: True
    reduction: 'mean'
  group_args:
    NAME: 'ballquery'
    use_xyz: True
    normalize_dp: True
  conv_args:
    order: conv-norm-act
  act_args:
    act: 'relu'
  norm_args:
    norm: 'bn'
decoder_args:
  NAME: PointNet2Decoder
  fp_mlps: [[64, 64], [128, 128], [256, 256], [512, 512]]

```

Listing 3: AssaNet Configuration

```

NAME: BaseSeg
encoder_args:
  NAME: PointNextEncoder
  blocks: [1, 2, 3, 2, 2]
  strides: [1, 4, 4, 4, 4]
  width: 64
  in_channels: 3
  sa_layers: 1
  sa_use_res: True
  radius: 0.1
  radius_scaling: 2.5
  nsample: 32
  expansion: 4
  aggr_args:
    feature_type: 'dp_fj'
    reduction: 'max'
  group_args:
    NAME: 'ballquery'
    normalize_dp: True
  conv_args:
    order: conv-norm-act
  act_args:
    act: 'relu' # leakrelu makes training unstable.
  norm_args:
    norm: 'bn' # ln makes training unstable
decoder_args:
  NAME: PointNextDecoder

```

Listing 4: PointNeXt Configuration

```

NAME: BaseSeg
encoder_args:
  NAME: PointViT
  in_channels: 3
  embed_dim: 512
  depth: 8
  num_heads: 8
  mlp_ratio: 4.
  drop_rate: 0.
  attn_drop_rate: 0.0
  drop_path_rate: 0.1
  add_pos_each_block: True
  qkv_bias: True
  act_args:
    act: 'gelu'
  norm_args:
    norm: 'ln'
    eps: 1.0e-6
  embed_args:
    NAME: P3Embed
    feature_type: 'dp_df'
    reduction: 'max'
    sample_ratio: 0.0625
    normalize_dp: False
    group_size: 32
    subsample: 'fps' # random, FPS
    group: 'knn'
    conv_args:
      order: conv-norm-act
      layers: 4
      norm_args:
        norm: 'ln2d'
  decoder_args:
    NAME: PointViTDecoder
    channel_scaling: 1
    global_feat: cls,max
    progressive_input: True

```

Listing 5: PointBERT Configuration

B.3 FIGConvNet Configuration

We share the network configuration used in FIGConvNet experiments in the appendix. The code will be released upon acceptance, and the network configuration below uniquely defines the architecture.

B.4 FIG ConvNet Architecture Details

In this section, we provide architecture details used in our network using the configuration files used in our experiments.

```

num_levels: 2
kernel_size: 5
hidden_channels:
  - 16
  - 32
  - 48
num_down_blocks: [1, 1] # defines the number of FIGConv blocks
                    per hierarchy in encoder
num_up_blocks: [1, 1] # defines the number of FIGConv blocks
                    per hierarchy in decoder
resolution_memory_format_pairs: # defines the grid resolutions
  - [ 5, 150, 100]
  - [250, 3, 100]
  - [250, 150, 2]

```

Listing 6: **FIGConvNet Configuration**

B.5 Warp-based Radius Search

The algorithm 1 describes how we efficiently find the input points within the radius of a query point in parallel. It follows the common three-step computational pattern in GPU computing when encountering dynamic number of results: Count, Exclusive Sum, Allocate, and Fill. We achieve excellent performance by leveraging NVIDIA’s Warp Python framework, which compiles to native CUDA and provides spatially efficient point queries with its hash-grid primitive.

Procedure 1 GPU-accelerated points in a radius search

Input: input points p , query points q , radius r

Output: Results Array, Result Offset

procedure COUNTRADIUSRESULTS(query points, input points, radius r)

 Step 1: Count number of results

for all query points q **do**

while candidate $p \leftarrow$ hash-grid query(q, r) **do**

if $\|q - p\| < \text{radius}$ **then** count[q] $++$

end if

end while

end for

end procedure

procedure COMPUTEOFFSET(count)

 offset \leftarrow exclusive-sum(count)

 total number results \leftarrow offset[last]

 results-array \leftarrow alloc(total number results)

end procedure

procedure FILLRADIUSRESULTS(query points, input points, radius r , offset)

for all query points q **do**

 q-count \leftarrow 0

while candidate $p \leftarrow$ hash-grid query(q, r) **do**

if $\|q - p\| < \text{radius}$ **then**

 results-array[offset[q-count]] \leftarrow p

 q-count $++$

end if

end while

end for

end procedure

procedure POINTSINRADIUS(input points, query points, radius)

 count \leftarrow COUNTRADIUSRESULTS(query points, input points, radius)

 offset, allocated results array \leftarrow COMPUTEOFFSET(count)

 results array \leftarrow FILLRADIUSRESULTS(query points, input points, radius, offset, results array)

end procedure
